JACS
JOURNAL OF THE AMERICAN CHEMICAL SOCIETY
pubs.acs.org/JACS
Article

Evaluating the Catalytic Efficiency of the Human Membrane-type 1 Matrix Metalloproteinase (MMP-14) Using AuNP–Peptide Conjugates

Zhicheng Jin, Narjes Dridi, Goutam Palui, Valle Palomo, Jesse V. Jokerst, Philip E. Dawson, Qing-Xiang Amy Sang, and Hedi Mattoussi*

Cite This: J. Am. Chem. Soc. 2023, 145, 4570–4582
Read Online

ACCESS | Metrics & More | Article Recommendations | Supporting Information

ABSTRACT: Interactions of plasmonic nanocolloids such as gold nanoparticles and nanorods with proximal dye emitters result in efficient quenching of the dye photoluminescence (PL). This has become a popular strategy for developing analytical biosensors relying on this quenching process for signal transduction. Here, we report on the use of stable PEGylated gold nanoparticles, covalently coupled to dye-labeled peptides, as sensitive optically addressable sensors for determining the catalytic efficiency of the human matrix metalloproteinase-14 (MMP-14), a cancer biomarker. We exploit real-time dye PL recovery triggered by MMP-14 hydrolysis of the AuNP–peptide-dye to extract quantitative analysis of the proteolysis kinetics. Sub-nanomolar limit of detections for MMP-14 has been achieved using our hybrid bioconjugates. In addition, we have used theoretical considerations within a diffusion-collision framework to derive enzyme substrate hydrolysis and inhibition kinetics equations, which allowed us to describe the complexity and irregularity of enzymatic proteolysis of nanosurface-immobilized peptide substrates. Our findings offer a great strategy for the development of highly sensitive and stable biosensors for cancer detection and imaging.

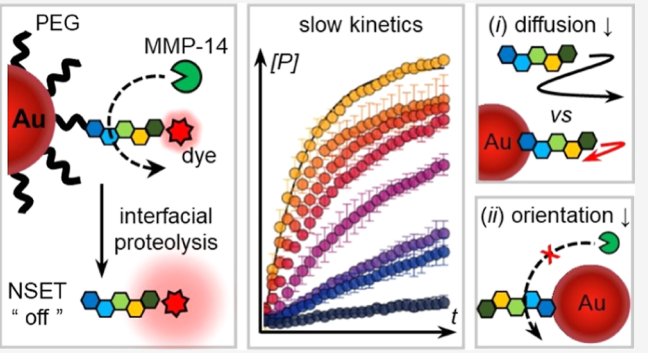

Downloaded via FLORIDA STATE UNIV on April 10, 2023 at 21:33:45 (UTC).
See https://pubs.acs.org/sharingguidelines for options on how to legitimately share published articles.

INTRODUCTION

Proteases are known to be implicated in many human diseases and disorders, such as cancer and stroke.[1,2] They have significant value in diagnostics and are important pharmaceutical targets. For example, the matrix metalloproteinase-14 (MMP-14), also known as membrane-type 1 matrix metalloproteinase (MT1-MMP), is involved in regulating breast cancer progression and allowing tumor cells to escape and metastasize.[3] Established tools for probing MMP-14 include enzymatic, immunochemical, electrochemical, and optical biosensors.[4−8] A popular sensing platform relies on assembling two fluorophores (a donor and an acceptor) flanking a spatial linkage that acts as a substrate for the target analyte(s).[6,9−11] Such sandwich configuration takes advantage of the exquisite sensitivity of fluorescence resonance energy transfer (FRET) interactions to nanometer-scale changes in the donor–acceptor distance.[9,10,12,13] Recently, fluorescent semiconductor nanocrystals (quantum dots, QDs) have been exploited as unique FRET-based energy donors to sense a few key enzymes.[14−16] Though effective, QD-sensors suffer from the stigma associated with potential cytotoxicity ascribed to the presence of heavy metals in their cores (e.g., Cd or Te).[17−19]

Gold nanoparticles (AuNPs), in comparison, exhibit remarkable stability, biocompatibility, tunable surface properties, and high translational values, which make them attractive candidates for developing biosensors.[5,20−25] The strong near–field interactions of AuNPs with proximal fluorophores result in efficient PL quenching.[26−29] The quenching efficiency exhibits a $1/R^4$ dependence on the separation distance (R) via nanometal surface energy transfer (NSET).[26,27,30] Experimentally, a few studies have exploited the reported coordination affinity of imidazole to assemble AuNP-bioconjugates via direct binding of biomolecules onto the AuNP surfaces.[20,31−35] Though easy, this conjugation strategy is difficult to implement when starting with ligand-protected surfaces, as this could lead to undesirable inactive low-quality conjugates due to a stable and thick ligand shell.[35,36]

Here, we have designed three sets of AuNP–peptide conjugates and applied them as optically addressed sensors to evaluate the enzyme activity of MMP-14. Two of the

Received: November 12, 2022
Published: February 20, 2023

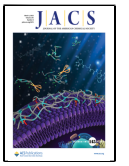

ACS Publications
© 2023 American Chemical Society

https://doi.org/10.1021/jacs.2c12032
J. Am. Chem. Soc. 2023, 145, 4570–4582

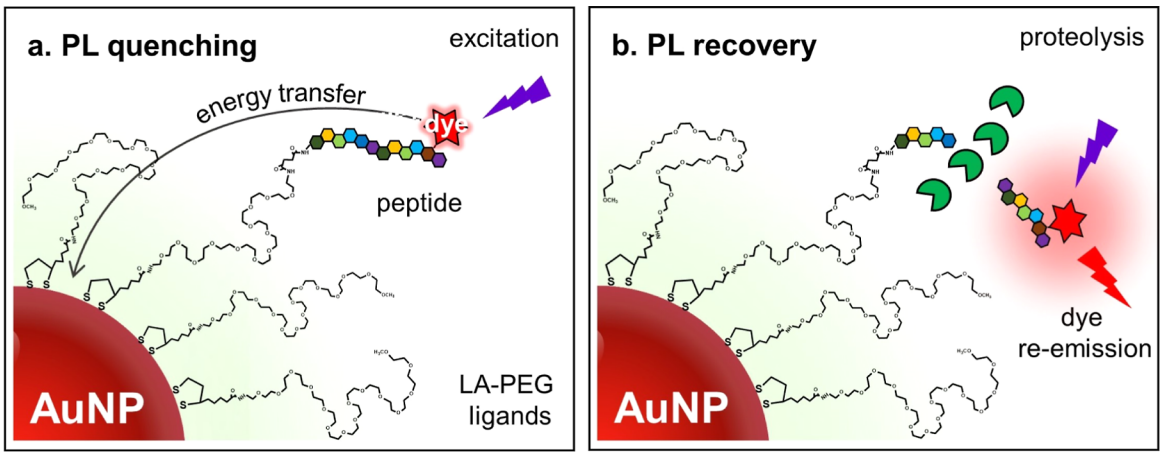

Figure 1. Schematic representation of the AuNP-peptide-dye conjugate used for sensing MMP-14 activity. (a) In the absence of enzymes, the dye PL is highly quenched due to its close proximity to the AuNP surfaces. (b) Upon incubation with the enzyme, proteolytic cleavage of the peptides releases the dyes, reducing nanometal surface energy transfer (NSET) interactions and promoting recovery of the PL signal.

Table 1. Peptide Information

Peptide name	Sequence	M.W. (g mol^{-1})	Protease
FS-6	H_2N–GGRPLG↓LYARAACA–$CONH_2$	1373.7	MMP-14
A-42	H_2N–GASGRIGF↓LRTAACA–$CONH_2$	1449.7	MMP-14
FS-6*	H_2N–ggrplglyaraaca–$CONH_2$	1373.7	N/A

[a] H_2N–surface coupling site; G and A–spacer; ↓–enzyme recognition site; C–dye coupling site

peptides contain a specific sequence each recognized by the enzyme, while the third provides a control. These bioconjugates have been assembled by chemically coupling tetramethylrhodamine (TAMRA)-labeled peptides to the surface passivating/coating PEG ligands (see Figure 1). The TAMRA dye choice is motivated by the sizable spectral overlap with the AuNP absorption, making this NSET-pair a desirable tool for protease detection via PL modulation. We have found that all AuNP-dye conjugates exhibit pronounced and valence-independent PL quenching efficiencies (up to ~85%). Our results also indicate that a near complete (~90%) hydrolysis of the surface-docked peptides and a fourfold PL enhancement in the presence of MMP-14 can be realized. The determined detection limit ranges from 0.05 to 1.60 nM. Additionally, we have found that the addition of an MMP inhibitor to the sample prevents any PL recovery. The two conjugates assembled using specific peptide substrates show slow enzymatic kinetics, with measured catalytic efficiency, k_{cat}/K_M, ~50–200-fold smaller than values reported using free peptides in solution. We combine our findings with literature data to gain new insights into how decoration of an AuNP scaffold with several peptides to form hybrid conjugates, combined with peptide crowding on the colloid, could change the substrate diffusion and reduce the rate of enzyme proteolysis.

RESULTS AND DISCUSSION

Conjugate Design and Assembly. The Au nanocrystals used in this study were grown using high temperature reduction of Au precursor under hydrophobic conditions, yielding homogenous oleylamine-capped AuNPs (d = 9.7 ± 2.1 nm); details about the growth along with TEM data (see Figure S1) are provided in the Supporting Information.[37] Ligand substitution, phase transfer, and surface functionalization of the nanoparticles were implemented via a rapid photoligation strategy using a mixture of methoxy- and carboxyl-appended lipoic acid (LA)-PEG ligands (i.e., the molar ratio of LA-PEG_{750}-OCH_3:LA-PEG_{600}-COOH = 4:1).[36,38,39] This yielded a PEG coating with 20% of the total number of ligands presenting active carboxyl groups (referred to as AuNP–COOH). The as-prepared PEGylated AuNPs showed excellent long-term colloidal stability over a wide range of biological conditions.[23,40−42] Subsequently, AuNP-peptide-dye conjugates with a strong and controlled PL quenching were obtained by coupling the lateral –COOH groups to the peptide-dye via the EDC [1-ethyl-3-(3-dimethylaminopropyl)carbodiimide] condensation reaction.[43]

We custom-designed two modular peptides (FS-6 and A-42) that contain substrate sequences for MMP-14, and which can be readily integrated into the AuNP-conjugate assemblies.[44−46] Precisely, the modular peptides contain four functional domains (Table 1): (i) a N-terminal amine for covalent coupling to the AuNP–COOH; (ii) a spacer consisting of alternating glycine (G) and alanine (A) residues; (iii) a MMP-14 cleavage site; and (iv) a cysteine (C) near the C-terminus for dye labeling via sulfhydryl-maleimide chemistry.[47,48] Peptide amidation and substitution of lysine residues (K) with arginine (R) in FS-6 and A-42 peptides were employed to avoid secondary reactions during the EDC condensation step. In addition to the above peptides, a D-amino acid peptide (FS-6*) was also designed and synthesized as an internal non-cleavable control. The structure of these synthetic peptides along with the cleavage sites were confirmed using MALDI-TOF mass spectrometry (MS), with a representative example (FS-6) shown in Figure 2.

The red-emitting TAMRA dye has a sizable spectral overlap with the AuNP absorption, which promotes strong NSET interactions and thus efficient PL quenching (Figure 3a).[27,29]

https://doi.org/10.1021/jacs.2c12032
J. Am. Chem. Soc. 2023, 145, 4570−4582

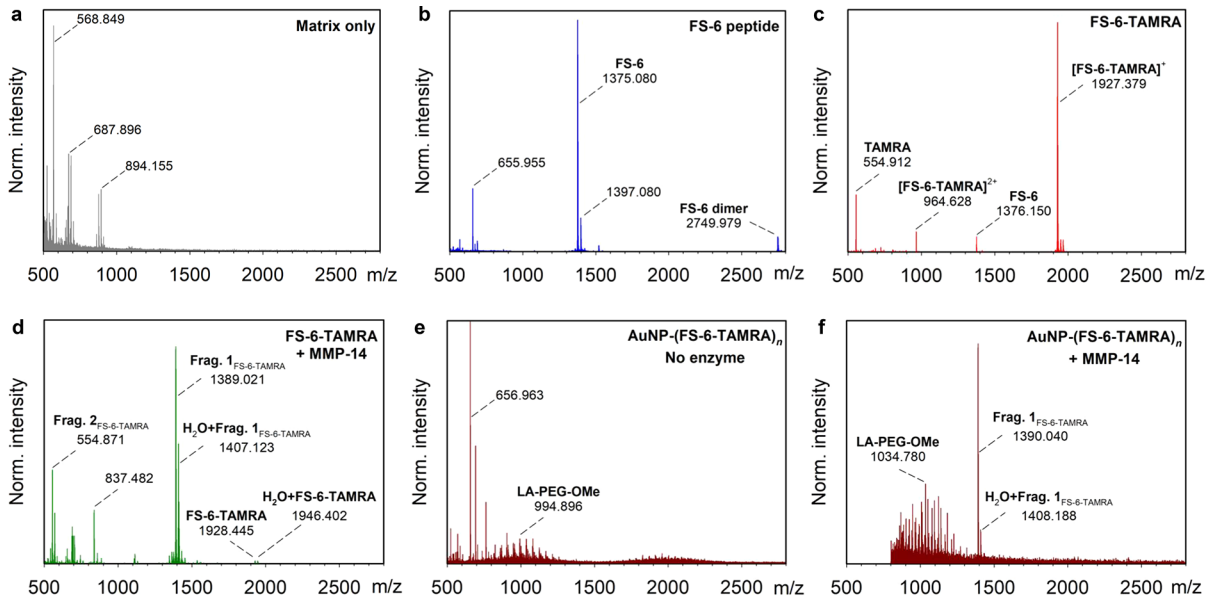

Figure 2. MS characterization of peptide-dye labeling. MALDI-TOF MS spectra acquired from: (a) the matrix only, as a control; (b) FS-6 peptide; (c) TAMRA-labeled FS-6 peptide (or FS-6-TAMRA); (d) solution of the FS-6-TAMRA after incubation with MMP-14 for 2 h. The conditions used were 37 °C, sodium phosphate buffer pH 7.5, and $[S]_0/[E]_0$ = 400:1. We should note that the peak at 837.482 represents the fragment emanating from digestion of the small fraction of TAMRA-free peptide in the sample, as shown in (c). The disappearance of the parent FS-6, along with the emergence of the new fragments imply a complete peptide digestion. They also indicate that TAMRA labeling did not alter the biological activity of the FS-6 peptide. (e) MS spectrum acquired from AuNP−$(FS\text{-}6\text{-}TAMRA)_n$ after size exclusion chromatography, showing no detectable signal from the free peptide-dye. (f) Data acquired from the AuNP conjugates after enzyme assay, showing a peak ascribed to the free dye-peptide fragment.

Prior to AuNP−peptide-TAMRA formation, TAMRA was first linked to the peptide via cysteine-maleimide chemistry. Figure 2 shows the successful dye-labeling of the peptide as verified using MALDI-TOF MS. The AuNP−peptide-TAMRA conjugates were then prepared by attaching the peptide terminal amine to AuNP−COOH through an EDC/NHS coupling reaction.[43] The optimal molar ratio of EDC/NHS was 4:1; further details on the conjugation are provided in the Supporting Information. The AuNP-conjugates were purified by size-exclusion chromatography (using a PD-10 column), and collecting the first elution band. Figure 2e confirms that the MS data from the purified assemblies shows no signal from the free peptide-dye. Images of the dispersions of AuNP-dye conjugates under white-light and UV-illumination show enhanced TAMRA emission at high valence (Figure S3).

Characterization of the Conjugates. The polyvalent AuNP−$(peptide\text{-}TAMRA)_n$ conjugates were characterized by UV−vis absorption spectroscopy, mass spectrometry, fluorescence spectroscopy, and gel electrophoresis. Figure 3b shows the composite absorbance profile of AuNP−$(FS\text{-}6\text{-}TAMRA)_n$ and the deconvoluted contribution from AuNP and dye components. The valence, n, is defined as the average molar ratio of dye-to-NP in the conjugates. This is extracted by comparing the deconvoluted absorbance to their molar absorption coefficients, that is, $\varepsilon_{520\text{-}nm} = 6.58 \times 10^7\ M^{-1}\ cm^{-1}$ for AuNPs and $\varepsilon_{554\text{-}nm} = 8.0 \times 10^4\ M^{-1}\ cm^{-1}$ for TAMRA.[49] Overall, the absorption data show a progressive increase in the dye contribution to the composite spectrum that is commensurate with the equivalent concentration of peptide-TAMRA used, indicating a good control over the conjugate valence. Indeed, attaching a controllable number of peptide substrates to each AuNP increases the local substrate concentration, which may have important implications for sensor performance.[14,47]

The above results were further complemented by quantifying the fluorescence properties before and after coupling the dye-peptide to AuNPs. Figure 3c shows a substantial loss in the dye fluorescence after AuNP conjugation, ascribed to NSET interactions. These interactions are stronger than those attributed to Förster dipole−dipole interactions.[27,29,30] Using the PL spectra, we quantified the NSET quenching efficiencies, E_{NSET}, using

$$E_{NSET} = 1 - \frac{PL_{DA}}{PL_D} \quad (1)$$

where PL_D and PL_{DA} designate the PL of dye alone (donor, D) and AuNP-dye conjugates (donor−acceptor, DA), respectively. We also acquired fluorescence data from the dispersions made of mixtures of PEGylated AuNPs and free peptide-TAMRA (as control), which were used to account for the effects of collisional interactions. These interactions are always present but are much weaker than those measured for coupled AuNP-dye pairs.[33] Figure 3d shows the estimated E_{NSET} for several conjugates with a valence increasing from 0 to 70. Pronounced and valence-independent quenching efficiencies (~85%) were measured. As expected, a modest quenching efficiency was measured for the control experiments ($E_{collision}$ ~50%).[29,33] The combined observations validate the successful AuNP-peptide-dye conjugation, which brings TAMRA in close proximity to the plasmonic surfaces and thus results in a strong PL quenching. Notably, the NSET interactions between TAMRA dyes and the central AuNP in the assembled conjugates are simultaneous but not cumulative, as each fluorophore interacts individually with the metallic surfaces.[26]

https://doi.org/10.1021/jacs.2c12032
J. Am. Chem. Soc. 2023, 145, 4570−4582

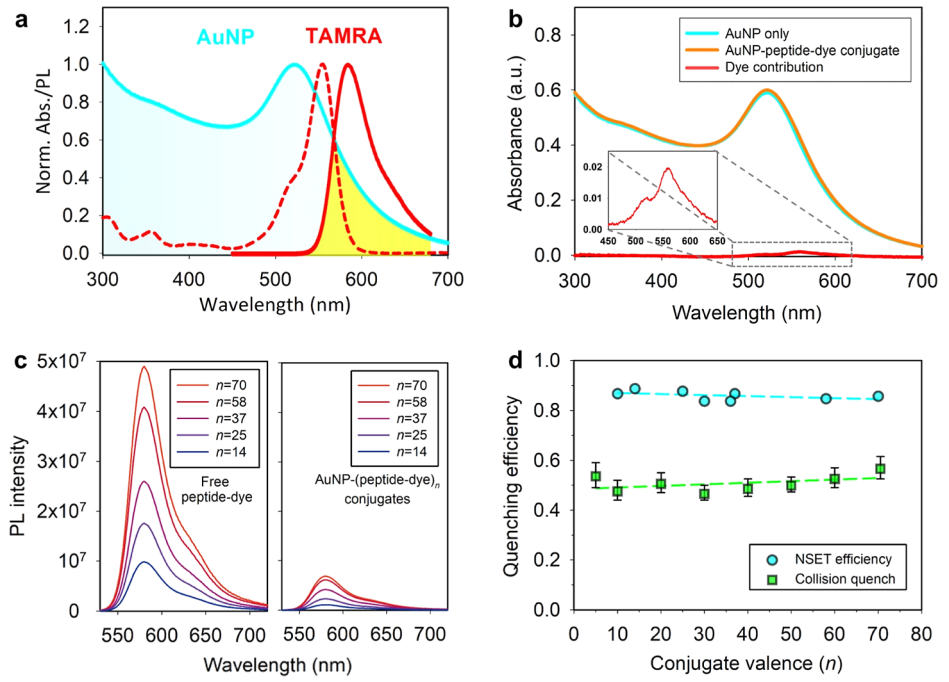

Figure 3. (a) Normalized TAMRA emission and absorption profiles (solid and dashed red lines), along with the AuNP absorption (cyan). The spectral overlap is shown in yellow. (b) Deconvolution of the composite absorbance spectrum of the AuNP−(peptide-TAMRA)$_n$ yields the AuNP and TAMRA dye contributions to the total absorbance. Inset shows a close view of the dye contribution. The conjugate valence, n, is extracted from the deconvoluted absorbance using the known molar absorption coefficients. (c) PL spectra collected from a solution of free peptide-TAMRA (PL_D, left) compared to a conjugate sample (PL_{DA}, right) at equivalent concentrations. Regardless of the valence numbers, the extracted quenching efficiencies are ∼85%. (d) Quenching efficiency measured for the conjugates (attributed to NSET, cyan-filled circles), side-by-side with the quenching measured for a mixture of AuNPs and free peptide-TAMRA to account for collision quenching (control, green-filled squares). The AuNP concentration was 10 nM, while the peptide-dye concentration was varied. Error bar = standard deviation (n = 3).

This explains both the strong and valence-independent quenching in our system.

The above optical data can be further exploited to convert changes in the PL signals to amounts of cleaved peptide during an enzyme assay, which in turn allows us to quantify the kinetic parameters of the proteolysis reaction. Digestion of the AuNP-peptide-dye conjugates displaces the cleaved dye-peptide fragments away from the AuNPs and produces a PL response that combines contributions from both freed dye-peptide-fragments (via collision interactions) and still surface-attached peptide dyes. To extract an accurate estimate for the molar amounts of cleaved peptides during proteolysis, we developed a calibration curve that correlates the concentration of cleaved dye-peptide fragments to the measured PL signal by monitoring the TAMRA emission for a series of mixtures containing free peptide-dye and AuNP−(peptide-dye)$_m$ conjugates with varying valences, while keeping a constant total molar ratio of dye-to-AuNP; the conjugate in the mixture m varies between 0 and 14. Figure 4 shows a standard curve (linear profile) corresponding to a fixed dye-to-AuNP molar ratio of 14. This linear fit was used to back-calculate the amount of cleaved product, [P], at different reaction times and build time-dependent enzymatic curves, which we have exploited for developing kinetic analysis.[14]

Enzyme Assays Using AuNP-Peptide Conjugates. The active site of an enzyme may contain a mixture of several states that can be affected by activation, purification, and long-term storage. It is thus important to accurately determine what the catalytically active fraction in the sample is. To implement this, we used tight-binding titration in the presence of a broad-spectrum MMP inhibitor, GM6001, where AuNP−(FS-6-TAMRA)$_{14}$ conjugates served as the titrants. Experimental details along with the analysis can be found in the Supporting Information (Figure S4). The data indicate that approximately 38% of the MMP-14 in the enzyme stock solution preserved their catalytic activity. The reported enzyme concentration will refer to the amount of active enzyme in the sample, unless otherwise indicated.

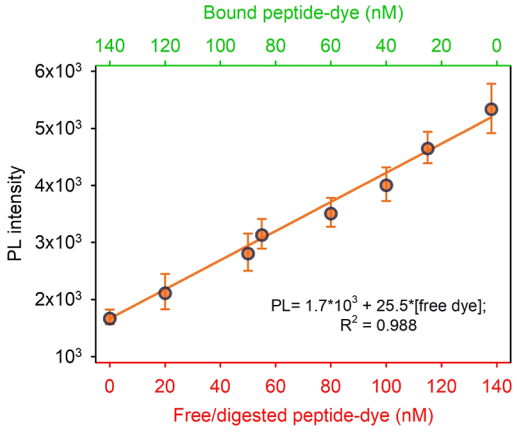

Figure 4. Standard curve correlating the PL intensity with the concentration of freed peptide-TAMRA. The PL is measured over mixtures of free peptide-dye and AuNP−(peptide-TAMRA)$_n$ assemblies, with the valence (n) varied from 0−14; [AuNP] = 10 nM. Error bar = standard deviation (n = 3). The data were best fitted using a linear function: $I_{PL} = 1.7 \times 10^3 + 25.5 \times [P]$; $R^2 = 0.988$.

The enzyme assays were performed using three sets of conjugates, namely AuNP−(FS-6-TAMRA)$_{14}$, AuNP−(A-42-

https://doi.org/10.1021/jacs.2c12032
J. Am. Chem. Soc. 2023, 145, 4570−4582

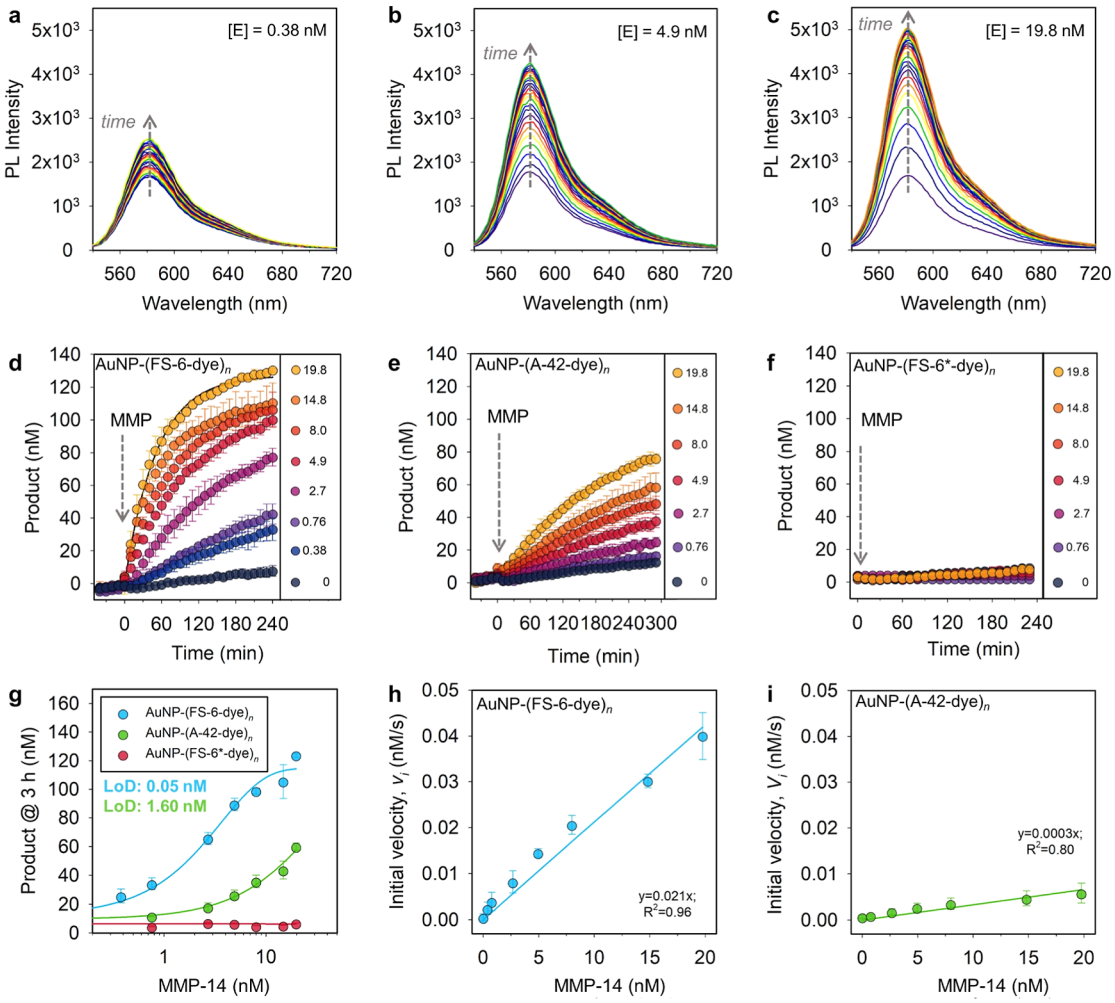

Figure 5. Enzyme assays using AuNP-peptide-dye. (a–c) Progression of the emission spectra was recorded every 10 min, where 10 nM of AuNP–(FS-6-TAMRA)$_{14}$ conjugates were incubated with various concentrations of MMP-14 (0–19.8 nM) and tracked with time. Shown are time-dependent digestion curves of: (d) AuNP–(FS-6-TAMRA)$_{14}$ over a period of 250 min, (e) AuNP–(A-42-TAMRA)$_{14}$ over a period of 300 min and (f) AuNP–(FS-6*-TAMRA)$_{14}$ over a period of 240 min, upon incubation with various concentrations of MMP-14. Data were plotted by converting the PL intensity at 580 nm into product concentration based on the calibration curve shown in Figure 4. Error bars = standard deviations (n = 2). The dashed arrow designates the MMP-14 addition. A fit of $[P]$ versus t at $[E]$ = 19.8 nM using Eq 3 is provided, see solid line. (g) Molar amount of product (at 3 h) as a function of MMP-14 concentration. The deduced LoD for MMP-14 is: 0.05 nM using AuNP–(FS-6-TAMRA)$_{14}$, and 1.60 nM using AuNP–(A-42-TAMRA)$_{14}$. (h–i) Plots of v_i vs $[E]$ for conjugates using FS-6 (h) and A-42 (i). The data are fitted using $v_i \approx (k_{cat}[S]_0/K_M)\cdot[E]$. Error bars = standard deviations (n = 2).

TAMRA)$_{14}$, and AuNP–(FS-6*-TAMRA)$_{14}$; all conjugates have a valence n = 14. A "varying enzyme assay" was applied, that is, a range of equivalent enzyme concentrations ($[E]_0$, from 0–19.8 nM) were incubated with a fixed substrate concentration in excess ($[S]_0$ = 140 nM). More precisely, aliquots of the conjugates were first mixed with kinetic buffer and left to pre-equilibrate for 50 min, followed by mixing with various amounts of enzyme solutions to reach the desired enzyme concentration in each sample. The dispersions were excited at 515 nm and emission spectra were collected using a fluorescence microtiter plate reader. Figure 5a–c shows a clear enhancement in the TAMRA PL with time that is commensurate with the enzyme concentration used, with up to fourfold signal recovery measured for the highest concentration (19.8 nM). This is triggered by interfacial hydrolysis of the surface-docked peptides, releasing dye-peptide segments and resulting in the loss of NSET interactions. The PL intensity centered at 580 nm, collected at each time interval, was converted to time-dependent proteolysis curves (i.e., $[P]$ vs. t, see Figure 5d–f), using the linear calibration curve shown in Figure 4. The proteolysis curves suggest that the AuNP–(FS-6-TAMRA)$_{14}$ conjugates exhibit a more sensitive response to MMP-14 than that exhibited by AuNP–(A-42-TAMRA)$_{14}$ conjugates. The limit of detection (LoD) reached for MMP-14 using the AuNP–(FS-6-TAMRA)$_{14}$ and AuNP–(A-42-TAMRA)$_{14}$ substrates are ≅ 0.05 and 1.60 nM, respectively (see Figure 5g). These values are clinically relevant, as nanomolar scale MMP levels have been measured in patient serum.[3,50,51] Indeed, higher local concentrations of active MMP-14 were measured at the membrane of metastatic cancer cells.[3] In comparison, data acquired using the control substrates, by incubating AuNP–(FS-6*-TAMRA)$_{14}$ bioconjugates with MMP-14 under the same conditions, show negligible PL enhancement over the time course; this proves the absence of any enzyme–substrate interactions for this peptide sequence (Figure 5f).

We next tested the capacity of the present AuNP–(FS–6-TAMRA)$_{14}$ construct to detect the activity of MMP-14 in a

https://doi.org/10.1021/jacs.2c12032
J. Am. Chem. Soc. 2023, 145, 4570–4582

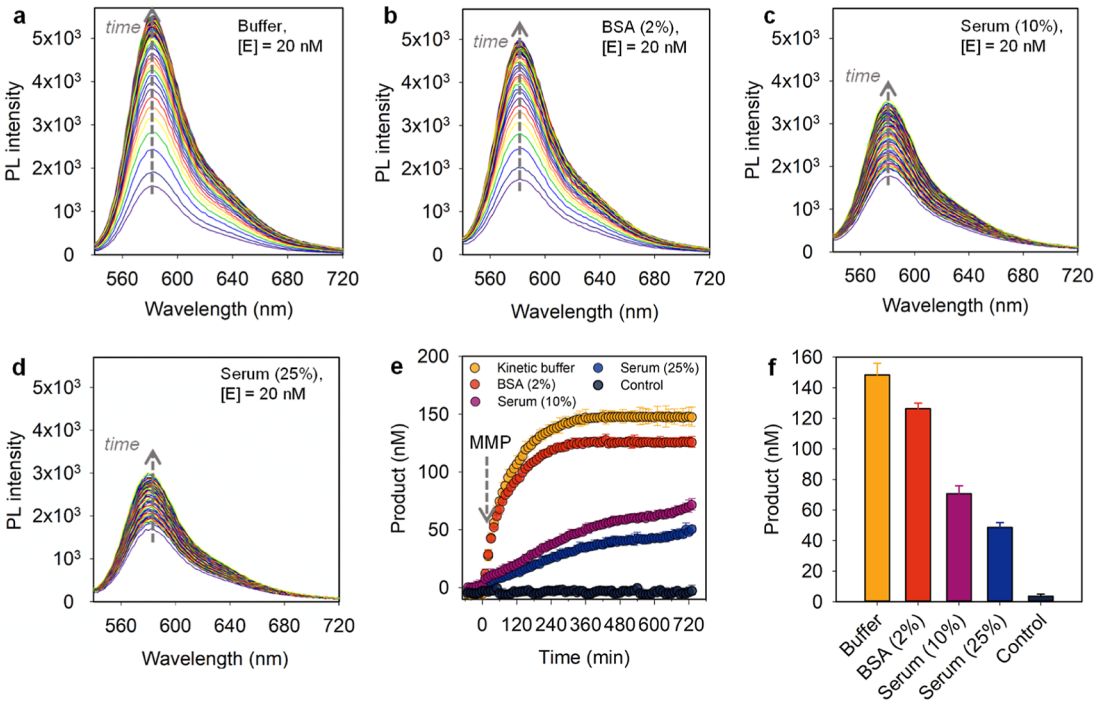

Figure 6. (a–d) Effects of the matrix used. Progression of the emission spectra recorded every 10 min, using 10 nM AuNP–$(FS\text{-}6\text{-}TAMRA)_{14}$ conjugates incubated with 20 nM MMP-14 in (a) HEPES buffer 50 mM, (b) HEPES buffer supplemented with 2% BSA, (c) 10% serum, and (d) 25% serum. Data for 0 nM MMP-14 in 10% serum, used as the control, are shown in Figure S5. (e) Digestion profiles extracted from the above spectra by converting the PL intensity at 580 nm into product concentration based on the calibration curve shown in Figure 4. Error bars = standard deviations (n = 2). The dashed arrow designates the MMP-14 addition. (f) Bar graphs for the product extracted from the PL intensity at 580 nm after incubating the AuNP–$(FS\text{-}6\text{-}TAMRA)_{14}$ conjugates with MMP-14 in different media for 12 h.

more biologically relevant medium, namely serum, under similar excess peptide conditions ($[S]_0$ = 140 nM). Figure 6 shows side-by-side the progression of PL recovery data acquired from solutions of the conjugates mixed with an enzyme concentration $[E]$ = 20 nM under several conditions. Included were solutions of: 50 mM kinetic buffer alone, buffer with 2% BSA, buffer with 10% Horse serum and buffer with 25% Horse serum. Additional recovery spectra acquired in 10% serum using $[E]$ = 0, 10, and 15 nM are shown in the Supporting Information (see Figure S5). Note that the recovery was tracked for 12 h, compared to those shown in Figure 5 (tracked for 4 or 5 h). Plots of the product versus time along with the maximum product measured under each condition are shown in panels 6e,f. Data show that the amount of digested peptide steadily decreased following the trend: kinetic buffer > 2% BSA solution > 10% serum > 25% serum. Data also show that though a drop in the enzyme activity was measured for all conditions compared to that measured in pure buffer, a sizable activity persisted under all those conditions. In particular, the profiles in panel 6f show that the products measured in 10 and 25% serum, at $[E]$ = 20 nM, are ~35 and ~50%, respectively, compared to that measured in pure buffer (see Figure 6f). The detection limit is comparable to that achieved in buffer. Cumulatively, these results prove that the present conjugates can be applied to biologically relevant samples. We would like to note that the lower MMP-14 activity measured in the serum solutions should be expected. It can be attributed to the presence of α-2-macroglobulin proteins (a known broad-spectrum protease inhibitor).[52] The α-2-macroglobulin inhibition relies on luring active proteases into its molecular cages and then flagging these complex for elimination.[52] With additional optimization of the conditions, better data could be easily acquired. These include the use of LA-zwitterion ligands to provide enhanced affinity of the conjugates to water while reducing the overall lateral size of the coating layer. This in turn provides better exposure of the tethered peptides and easier access of the catalytic domain to the cleavage site on the conjugates. Similarly, one can try to identify proteins that block the inhibitory effects of α-2-macroglobulin. One additional concern is the potential interference by nonspecific adsorption of proteins (corona formation). Though studies from our group and others have shown that PEGylated coating prevent corona buildup, the use of zwitterion ligands could further alleviate the effects of nonspecific adsorption on NP-conjugates, if present.[53,54]

A few key findings can be deduced from the above experiments: (i) The AuNP–$(peptide\text{-}TAMRA)_n$ hybrids are stable and stay active over the tested conditions, prior to the addition of MMP-14 (Figure 5d–f). Importantly, the assembled conjugates preserve their sensing functions for up to 1 month of storage at 4 °C. (ii) Our data show high sensitivity of the AuNP–$(FS\text{-}6\text{-}TAMRA)_{14}$ assemblies to MMP-14 at sub-nanomolar concentrations, with over 90% of the docked peptides catalyzed at higher enzyme concentrations. This can be ascribed to the easy access of the enzyme catalytic domain to the surface-bound substrates in the assembly. (iii) There is a clear specificity in the interactions exhibited by different substrates embedded in the conjugates toward MMP-14, as anticipated from previous data.[44−46] For example, assays employing AuNP–FS-6 conjugates yield a hydrolysis rate (or amounts of catalytic products) that are at least twofold larger than those measured for A-42 peptide (compare 5d and 5e). These features highlight the modular peptide design, the spatial separation between the AuNP

https://doi.org/10.1021/jacs.2c12032
J. Am. Chem. Soc. 2023, 145, 4570−4582

surface and the substrate sequence, and the benefits of inserting a PEGylated linker between the NP and the peptide, all combined with the effectiveness of NSET as a transduction mechanism to report on the proteolysis process. The importance of a PEG_{600} bridge/linker is twofold. It eliminates potential screening of attached peptides if no or a much shorter PEG bridge is used to couple the substrate. It also provides a better-exposed reactive domain on the tethered peptide, which in turn facilitates easy enzyme access to the NP-conjugates and a higher rate of digestion. Our group has shown that using short reactive ligands (e.g., LA-TEG-COOH or LA-TEG-amine) mixed with LA-PEG_{750}-OMe, reduces the coupling efficiency of targeted dyes and metal complexes and ultimately results in reduced energy transfer or charge transfer interactions for NP-dye/metal complex conjugates.[55] Additionally, a recent study by Jokerst's group has looked into using peptides as substrates and a hydrophilic coating on AuNPs.[56] In particular, the authors explored two configurations: In one configuration, the peptides were directly coordinated onto the NP surface, while in the other peptides containing a linker/bridge between the binding domain and the active substrate sequence were attached onto the AuNPs. They indeed measured a drastically reduced enzyme proteolysis when using AuNP-peptide conjugates devout of a linker. This clearly proves our point that the insertion of the PEG linker between the LA anchors on the NP and the substrate is critically important for sensor functions. Finally, we should note that because solution samples are used our present design has the potential to be readily applied to cellular and other in vivo studies.

To better understand and exploit the data acquired for MMP-14, we consider the effects of sample configuration, namely the presence of several tethered peptides and how that would impact the enzyme−substrate interactions and the ensuing proteolysis and its kinetics.

Interfacial Enzyme Kinetics. In the simplest scheme, enzyme digestion of a substrate involves two steps, enzyme−substrate complex formation followed by digestion of the substrate, yielding the product and free enzyme, where the overall reaction is in general expressed as:

$$\mathrm{E} + \mathrm{S} \underset{K_{off}}{\overset{K_{on}}{\rightleftharpoons}} \mathrm{ES} \underset{K_{-cat}}{\overset{K_{cat}}{\rightleftharpoons}} \mathrm{E} + \mathrm{P} \tag{2}$$

In our case, the peptide substrates have been immobilized on AuNP surfaces. To maintain some of the key assumptions used in the Michaelis−Menten (MM) model, we have applied the "varying enzyme assay" format and used the standard quasi-steady-state assumption (sQSSA) in our analysis, where the concentration of enzyme-complexed substrate, [ES] stays constant (see Supporting Information, Section 8.3). The time-integrated MM equation under these conditions yields a simple expression for the product buildup with time

$$[P] = [S]_0 \cdot (1 - e^{-K_{obs} \cdot t}) \tag{3}$$

where the first-order rate constant K_{obs} is expressed as[46]

$$K_{obs} = \frac{k_{cat}[E]}{K_M + [E]} \tag{4}$$

The MM constant K_M appearing in Eq 4 is defined as $K_M = (k_{cat} + k_{off})/k_{on}$. Equation 3 can easily fit the experimental profiles for $[P]$ vs t at each enzyme concentration, $[E]$; two representative fits for $[E]$ = 19.8 nM are shown in Figure 5d,e. A close examination of Eq 3 indicates that the term K_{obs} is directly related to the initial velocity, via

$$v_i = \left(\frac{d[P]}{dt}\right)_{t=0} = [S]_0 \cdot K_{obs} \tag{5}$$

An additional simplification of Eq. 5 can further be applied using the condition ($K_M \gg [E]$) to yield a relationship for the initial velocity versus enzyme concentration that involves the catalytic efficiency of the enzyme, k_{cat}/K_M, and expressed as[46]

$$v_i \approx \frac{k_{cat}[S]_0}{K_M} \cdot [E] \tag{6}$$

Experimentally, v_i was extracted from the experimental digestion data limited to 15% substrate depletion. Figure 5h,i shows graphs of v_i vs $[E]$ for the two sets of AuNP-peptide conjugates. A linear profile is generated, which can be used to extract an average estimate for the catalytic efficiency using Eq 6 and the value for $[S]_0$, with $k_{cat}/K_M \cong$ 25,100 and 4,300 M^{-1} s^{-1} for AuNP−$(FS\text{-}6\text{-}TAMRA)_{14}$ and AuNP−$(A\text{-}42\text{-}TAMRA)_{14}$ conjugates, respectively. Our assay format does not allow the individual values for k_{cat} and K_M to be determined independently because the substrate concentration is lower than K_M, namely, $[S]_0 < 3\ K_M$; (we used the literature value of K_M).[14,57] For reference, the reported catalytic efficiencies reported for free FS-6 and A-42 peptides in solution were 1,253,000 and 777,200 $M^{-1}{\cdot}s^{-1}$, respectively.[45,46] The data shown above indicate that the catalytic efficiency measured using the peptides tethered onto AuNP surfaces exhibited approx. 50- to 180-fold reduction compared to free substrates in solution. We would like to note that the reduction in the enzyme catalytic efficiency (namely for MMP-14) was also measured using peptides that have been covalently coupled to luminescent PEG-stabilized QDs combined with changes in the fluorescence resonance energy transfer (FRET) interactions.[58]

We ascribe the reduction in the catalytic efficiency measured for the enzyme using our conjugates to the sample configuration. A more appropriate interpretation should consider a rigorous evaluation of the biomolecular activities for free versus NP-tethered peptides. We consider the effects of surface crowdedness combined with substantially reduced substrate mobility (in AuNP-conjugates) and argue that the configuration in question does not permit multiple enzymes to simultaneously or sequentially catalyze several peptides in a conjugate, which ultimately reduces the frequency of enzyme-to-substrate encounters. In such conjugates, the close proximity of substrates is smaller than the cross-section of the enzyme dimensions.[59] Below, we briefly discuss the effects of steric crowding and reduced substrate mobility when AuNP-tethered peptides are used. Additional details on a modified MM model that considers the effects of surface jamming are provided in the Supporting Information (Figure S6 and Section 8.4).

Collision-Diffusion Framework. The difference in the catalytic efficiency (k_{cat}/K_M) measured for MMP-14 using nanoparticle-peptide substrates, compared to the case where the substrates are freely diffusing in solution, may be attributed to differences in the encounter frequency between the enzyme molecules and peptide substrates in the two configurations. These differences can be conceptually formalized by considering the effects of the conjugate size and Brownian motion on the encounter frequency. Our group and others

https://doi.org/10.1021/jacs.2c12032
J. Am. Chem. Soc. 2023, 145, 4570−4582

have shown that the diffusion coefficient of the NP-bound ligands can be 2- to 10-fold smaller compared to free ligands.[60,61] This is important for enzymatic proteolysis involving NP-tethered substrates, as schematically shown in Figure 7. *We focus on two aspects: encounter frequency and reactant orientation.*

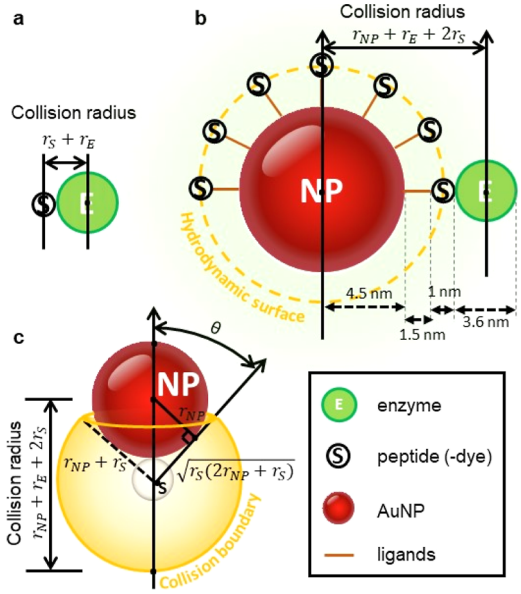

Figure 7. Interfacial enzyme kinetic model. The parameters used in estimating encounter frequency and steric requirement within a diffusion-collision framework. The collision radius for (a) a free substrate and enzyme in solution is $r_S + r_E$; (b) surface-docked substrates and a free enzyme is estimated to be $r_{NP} + r_E + 2r_S$. The fraction of reactive surface area on a conjugate is $\alpha \approx n\pi r_s^2/[4\pi(r_{NP} + r_s)^2]$. (c) The steric requirement of a free-substrate versus a bound-substrate decreases from 2π to $2\pi - 2\theta$. The shielding factor, η, is defined as P'/P [or $(\pi - \theta)/\pi$]. Note that $r_{NP} \approx$ 4.5 nm, $d_{PEG} \approx$ 1.5 nm,[55] $d_S \sim$ 1.0 nm,[47] and $d_E \approx$ 3.6 nm.

Aspect 1: Reduced Encounter Frequency. In this model, we make the following assumptions: (i) the NP, enzyme, and peptide substrates are abstracted as spherical objects; and (ii) the same activation energy, E_a, controls the reaction of soluble MMP-14 with either free or NP-bound peptide. Therefore, the encounter frequency for NP-tethered substrates, Z'_{on}, for the forward reaction can be expressed as[62−64]

$$Z'_{on} = \overline{V}' \cdot \frac{[E]}{2} \cdot ([NP] \cdot 4\pi r'^2 \alpha \cdot \gamma) \tag{7}$$

where $\overline{V'}$ is the relative mean speed of the colliding spheres of enzymes and AuNP conjugates (see Supporting Information, Section 8.5) and $[E]/2$ accounts for the fact that only half of the total enzymes are diffusing toward the conjugate for a given orientation and contribute to the total number of encounters. The second part in Eq 7 accounts for the total reactive surface area on a NP (Figure 7b), where α is the fraction of the AuNP surface decorated with the peptides and γ being the fraction of substrates available for enzyme complexation. r' designates the collision radius involving enzymes interacting with AuNP−peptide conjugates. Conversely, the encounter frequency for the freely diffusing peptide and enzyme is given by

$$Z_{on} = \overline{V} \cdot \frac{[E]}{2} \cdot \gamma [S]_0 \cdot 4\pi r^2 \tag{8}$$

where $\overline{V}$ is the relative mean speed of the colliding spheres of enzyme and substrate and r is the collision radius (see Figure 7a). Note that the expression of the relative mean speed of the colliding enzyme with either free or AuNP-tethered peptide is developed using the Maxwell distribution function of speeds and depends only on the lowest mass of the colliding pair. For example, $\overline{V}' = \left(\frac{8kT}{\pi m_E}\right)^{1/2}$ and $\overline{V} = \left(\frac{8kT}{\pi m_S}\right)^{1/2}$.[64] Additionally, the dependence of the forward rate constants, k'_{on} on Z'_{on} and k_{on} on Z_{on}, are assumed to follows an Arrhenius law[64]

$$k'_{on} = (Z'_{on} \cdot P') \cdot (e^{-E_a/RT}) \tag{9a}$$

and

$$k_{on} = (Z_{on} \cdot P) \cdot (e^{-E_a/RT}) \tag{9b}$$

where P and P′ represent the steric requirements for each configuration (see Aspect 2: Restrictions Due to Orientational Effects section below) and E_a is the activation energy. Therefore, the rate of ES formation (or k'_{on}) involving interactions with tethered substrate is much smaller than the one anticipated for freely diffusing substrate and enzyme (k_{on}), see Figure 7a vs. 7b.

Aspect 2: Restrictions Due to Orientational Effects. The AuNP−peptide-dye conjugate configuration imposes stringent steric requirements for promoting E−S complex formation and subsequent proteolysis (see Figure 7c). To account for this, a shielding factor, η, is introduced

$$\eta = \frac{P'}{P} = \frac{1}{2}\left[1 + \frac{\sqrt{r_S(2r_{NP} + r_S)}}{r_{NP} + r_S}\right] = 0.7 \tag{10}$$

where the various radii are defined in Figure 7 caption. Combining these steric requirements with differences in the diffusion coefficients, the model indicates that the estimated new forward rate, k'_{on}, between free enzyme and a NP-attached substrate is substantially smaller than k_{on}. For instance, at the early stage where $\gamma \approx 1$, the ratio k'_{on}/k_{on} is approx. 1/300.[65,66] These simple considerations provide a valuable insight into the decrease in the measured catalytic efficiency using our present conjugates compared to the freely diffusing peptide and enzyme. We therefore attribute the lower catalytic efficiency of the enzyme measured in our case to surface crowdedness, reduced collision frequency, and restricted reaction orientation. In particular, the substrate sandwich configuration (i.e., AuNP−peptide-dye) along with the reduced surface curvature of the AuNPs play a crucial role in reducing the catalytic efficiency by about 2 orders of magnitude compared to free diffusing enzyme and substrate.[48,65,66] The data shown in Figures 5 and 6 provide a first proof for the effects of reducing the collisional frequencies due to the slower diffusion of the conjugates compared to free peptides. In order to test the effects of crowding, we carried out one additional experiment where we increased the number of peptides tethered onto the AuNP while maintaining the same PEG-OMe and PEG-COOH mixture for surface stabilization and functionalization. More precisely, we carried out a digestion experiment using the conditions ([AuNP−peptide] = 10 nM and [E] = 20 nM). Note that the larger valence, extracted from the absorption data measured for the new sample as shown in Figure 2 and

https://doi.org/10.1021/jacs.2c12032
J. Am. Chem. Soc. 2023, 145, 4570−4582

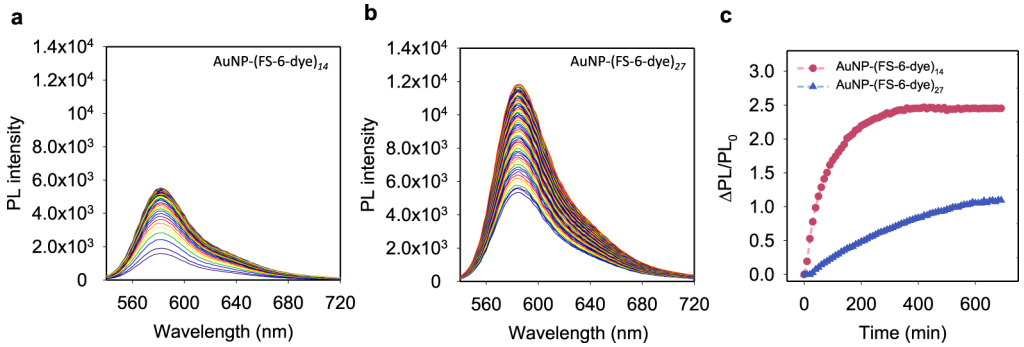

Figure 8. (a,b) Progression of the photoluminescence spectra was recorded every 10 min for a total period of 11 h. A conjugate concentration = 10 nM was used. Shown are data acquired using (a) AuNP−$(FS\text{-}6\text{-}TAMRA)_{14}$ and (b) AuNP−$(FS\text{-}6\text{-}TAMRA)_{27}$. Conjugates were incubated with 20 nM MMP-14 in 50 mM HEPES buffer. (c) Time-dependent progression of the relative PL change ($\frac{\Delta PL}{PL_0}$ vs time) for the dispersions of AuNP−$(FS\text{-}6\text{-}TAMRA)_{14}$ and AuNP−$(FS\text{-}6\text{-}TAMRA)_{27}$ conjugates upon incubation with MMP-14. The PL intensity at 580 nm is used for the two data sets in (a) and (b). The slow recovery of the relative PL changes measured for the AuNP−$(FS\text{-}6\text{-}TAMRA)_{27}$ conjugates indicates a lower rate of proteolysis, which we attribute to increased substrate crowding on the NP surfaces.

discussed above, increases the PL signal acquired before and during the digestion experiment. Extracting a curve for the product versus time cannot be accurately measured because that would require a new calibration curve (similar to Figure 4) for the new valence. Nonetheless, providing a direct side-by-side comparison on the relative increase in the PL recovery versus time for samples having 10 nM of AuNP−$(FS\text{-}6\text{-}TAMRA)_{14}$ and AuNP−$(FS\text{-}6\text{-}TAMRA)_{27}$ mixed with MMP-14 (at 20 nM) would directly account for differences in the catalytic efficiency for conjugates with different crowding parameters; the valence 27 is approx. 2 × 14 (see Figure 8). The condition $[E] \ll [S]_0$ is satisfied for both sample configurations. The relative PL recovery versus time clearly shows a markedly slower PL recovery and thus smaller digestion product with time for the higher valence (see Figure 8c). This result can be primarily attributed to the increased crowdedness expected for the sample of conjugates having a valence 27, with remnant effects of slightly modified diffusion due to the larger valence.

Finally, we would like to compare our findings to previous data. Overall, there are two configurations for testing the effects of integrating nanoparticles into an enzyme−substrate system. (i) In the first, a few enzyme proteins are immobilized onto nanoparticle surfaces and then tested for changes in the catalytic activity of the NP-enzyme assembly as it interacts with soluble peptide substrates. Studies have focused on testing the effects of NP size or/and curvature on the enzyme activity, when using this configuration.[66−70] (ii) In the second one, several peptide substrates are self-assembled around a nanoparticle (e.g., polyhistidine-appended peptides attached via meal-histidine coordination onto ZnS-overcoated quantum dots), and the nanoconjugates are allowed to interact with soluble freely diffusing enzymes. Here, authors have reported that overall, such configuration yields enhanced enzyme activity. In particular, ∼ threefold enhancement in the catalytic efficiency of trypsin was reported.[14] Our findings, namely, the decrease in the catalytic efficiency seem to agree with results measured for nanoparticle-tethered enzymes; our configuration involves NP-conjugated peptide substrates and free enzymes.[66−70] However, a comparison with an assay configuration involving QD-tethered peptides and freely diffusing enzyme, discussed in refs 14, 71−74 is conceptually more relevant. The strong reduction in the measured catalytic efficiency of MMP-14 using our assay format and nanosurface-immobilized peptides reported seems to disagree with literature data for Trypsin for example.[14,71−74] The assay format used in those studies varied the substrate molar amount via changes in the QD-conjugate concentration in order to satisfy the conditions of excess substrate. Possible explanations can be experimental factors, such as difference in the assay format, difference in the enzyme used and/or enzyme−peptide interactions, and conjugation strategy. We believe that our approach of relying on the varying enzyme assay format (under excess substrate conditions) provides data that are easier to analyze and yield a measure for the catalytic efficiency, K_{cat}/K_M, instead of individual parameters.

A few additional design modifications are under way in order to ultimately provide a more complete picture of the system. These include among others: (1) The use of different size AuNP platforms, which allow one to vary the Brownian diffusion and thus the encounter frequency between substrate and enzyme. (2) Substituting the solubilizing PEG_{750}-OMe with zwitterion motifs, which will provide a more compact coating and thus better exposure of the substrate on LA-PEG-peptide and more efficient interactions with the enzyme. (3) Varying the crowding properties of the peptide conjugates by using different ligand mixture combinations. We hope to report on those ideas in future reports.

■ CONCLUSIONS

We detailed the use of PEG-functionalized AuNPs, covalently coupled with three sets of dye-labeled peptides, as nanoprobes for solution-phase detection of the activity of MMP-14−a biomarker for human cancer. UV−vis absorption, steady-state PL, gel electrophoresis, and mass spectrometry measurements proved that several peptide-dye motifs were successfully coupled to an AuNP. The AuNP−peptide-dye assemblies exhibited significantly quenched dye PL, triggered by strong NSET interactions, which in turn allowed us to utilize them as probes for real-time monitoring the MMP-14 activity by tracking changes in the dye PL intensity during proteolysis. Indeed, systematic concentration- and time-dependent PL recovery of the conjugates upon incubation with varying concentrations of MMP-14 have been measured. Excellent sensitivity to proteolysis has been demonstrated, achieving detection of enzyme activity at sub-nanomolar range (i.e.,

https://doi.org/10.1021/jacs.2c12032
J. Am. Chem. Soc. 2023, 145, 4570−4582

0.05−1.60 nM). The PL recovery data were then quantitatively analyzed using a modified Michaelis−Menten model, yielding estimates for the catalytic efficiency for MMP-14. Notably, rather slow proteolysis was deduced for the configuration involving free enzymes interacting with several NP-tethered peptide substrates. Consideration of a diffusion-collision framework provided a few insights into the differences between our current system and those assays implemented without using nanoparticle scaffolds for immobilizing several copies of a substrate. This work sheds light on the subtleties of changing the local concentration of the peptide when employing free versus nanoparticle-conjugated substrates. Our findings can potentially lead to the development of protease detection and imaging sensors capable of evaluating the proteolytic activities of enzymes produced by cancer cells, bacteria, and other cells and organisms.

EXPERIMENTAL SECTION

PEGylation of AuNPs. Phase transfer and surface functionalization of the gold nanoparticles were carried out using a rapid UV-mediated ligand substitution strategy.[39,75] Typically, 200 μL of oleylamine-AuNP dispersion in hexane (0.67 μM) was precipitated with 2 mL of ethanol and centrifuged at 3,500 RPM for 5 min. The resulting NP pellet was then redispersed in 750 μL hexane using a scintillation vial. Next, a mixture of LA-PEG-OCH_3 (32 mg) and LA-PEG-COOH (7.3 mg) ligands was dissolved in 500 μL of MeOH and slowly added to the above vial. This corresponds to a molar ratio of LA-PEG-OCH_3:LA-PEG-COOH = 4:1, and a molar excess of ligands with respect to AuNPs of ∼300,000. A stir bar was introduced, and the content was placed inside the UV reactor and irradiated with a UV flux (with a peak centered at 350 nm) for 30 min. Following this, the reaction mixture was retrieved and stirred for 1 h. The gold colloids were precipitated by adding a mixture of hexane (3 mL) and $CHCl_3$ (500 μL), then centrifuged at 3,500 RPM for 5 min. The supernatant was discarded, and the reddish pellet was re-dispersed in 500 μL MeOH. Another round of precipitation was applied using a mixture of hexane and $CHCl_3$ and the pellet was slightly dried then dispersed in 4 mL of DI water. The dispersion was passed through a 0.45 μm syringe filter and further purified from excess ligands by applying 3 rounds of dilution/concentration using a membrane filtration device (Millipore, Mw cutoff = 100 kDa). The resulting dispersion was stored at 4 °C for future use. The molar extinction coefficient is $\varepsilon_{520\text{-nm}} = 6.58 \times 10^7\ M^{-1}\ cm^{-1}$ for AuNPs.[49]

Assembly of AuNP−(peptide-TAMRA)$_n$. The protocol for covalently attaching the N-terminus (−NH_2) of dye-labeled peptides to the AuNP−COOH via carbodiimide chemistry was optimized with regard to the EDC/NHS molar ratio and carboxyl activation time, based on literature protocols.[43] Here, we only describe the assembly of AuNP−FS-6-TAMRA, as the same procedure could be applied to prepare the other AuNP-bioconjugates. In a typical reaction, the AuNP−COOH dispersion (0.26 μM, 100 μL), DI water (50 μL), EDC·HCl (0.59 mg/20 μL DI water, assuming 120 −COOH per AuNP[75,76]), and NHS (0.09 mg/20 μL DI water, molar ratio of NHS:−COOH = 250) were mixed in a vial (final pH ∼6), yielding a molar ratio of EDC/NHS = 4:1. The mixture was stirred at room temperature for 10 min to activate the −COOH groups. Next, 100 μL of 20 mM PB (pH 10) was added to adjust the reaction to pH ∼8. Finally, 28 μL of the TAMRA-labelled FS-6 peptide (92 μM in PB, pH 7.5) was loaded, and the mixture was left stirring at room temperature overnight while protected from light exposure. The molar extinction coefficient of peptide-dye is $\varepsilon_{554\text{-nm}} = 8.0 \times 10^4\ M^{-1}\ cm^{-1}$. These conditions yield a peptide/AuNP molar ratio of ∼100:1 in the reaction mixture. The final dispersion was purified using a PD-10 desalting column (GE Healthcare) to remove uncoupled peptide-dye and excess reagents, using 50 mM kinetic buffer as an eluent. The first eluted band (500 μL) exhibiting a deep red color was collected and stored at 4 °C for further use.

Enzyme Assays. Prior to performing the assay, Aliquots of the AuNP−(FS-6-TAMRA)$_n$ conjugates (e.g., 40 μL, 22 nM) were pre-equilibrated with the desirable volumes of 50 mM kinetic buffer in a 96-well microtiter plate for ∼50 min at 27 °C, with intermittent 2 s mechanical shaking every 10 min until the PL signal was stabilized. Next, aliquots of the enzyme stock solution (335 nM) at desired volumes were pipetted into each well. Buffer was added to bring the total volume to 80 μL, and then the content was thoroughly mixed and homogenized. Fluorescence spectra were recorded over the range 540−720 nm every 10 min for a period exceeding 4 h, with excitation at 515 nm, using the Tecan Infinite M1000 microplate reader. Duplicate PL intensities were averaged and plotted against enzyme concentrations, and the standard error of the means was represented as error bars. The AuNP−(FS-6*-TAMRA)$_n$ was used as the control. The LoD calculation follows a reported statistical method[77]

$$\mathrm{LoD} = \mathrm{mean}_{\mathrm{blank}} + 1.645 \times (\mathrm{SD}_{\mathrm{blank}}) + 1.645 \times (\mathrm{SD}_{\mathrm{low\ concentration\ sample}}) \quad (11)$$

where SD is the standard deviation.

Enzyme Assays in Spiked Serum. We tested four different solution matrices, namely: 50 mM HEPES kinetic buffer, 50 mM buffer with 2% BSA, 10% Horse serum, or 25% Horse serum. First, the AuNP−(FS-6-TAMRA)$_{14}$ conjugates (e.g., 40 μL, 22 nM) were pre-equilibrated with the desirable volumes of the media in a 96-well microplate for ∼50 min at 27 °C, with intermittent 2 s mechanical shaking every 10 min, as done above. Next, 4 μL aliquots of the enzyme stock solution (400 nM) were pipetted into each well to a total assay volume of 80 μL, and then the content was thoroughly mixed and homogenized. The fluorescence spectra were recorded over the range 540−720 nm every 10 min for a period of 12 h using the microplate reader; sample excitation was at 515 nm. Duplicate PL intensities were averaged and plotted against enzyme concentrations, and the standard error of means was represented as error bars. The 0 nM MMP-14 was used as a control.

ASSOCIATED CONTENT

Supporting Information

The Supporting Information is available free of charge at https://pubs.acs.org/doi/10.1021/jacs.2c12032.

Materials, instrumentations, buffers, growth of AuNPs, ligand synthesis, NSET probe synthesis, gel electrophoresis, inhibitor assays, calibration curve, and enzyme kinetic background (PDF)

AUTHOR INFORMATION

Corresponding Author

Hedi Mattoussi − *Department of Chemistry and Biochemistry, Florida State University, Tallahassee, Florida 32306, United States;* orcid.org/0000-0002-6511-9323; Email: mattoussi@chem.fsu.edu

Authors

Zhicheng Jin − *Department of Chemistry and Biochemistry, Florida State University, Tallahassee, Florida 32306, United States;* Present Address: Department of NanoEngineering, University of California, San Diego, La Jolla, CA 92093, USA; orcid.org/0000-0001-6072-7533

Narjes Dridi − *Department of Chemistry and Biochemistry, Florida State University, Tallahassee, Florida 32306, United States;* orcid.org/0000-0001-9267-5475

Goutam Palui − *Department of Chemistry and Biochemistry, Florida State University, Tallahassee, Florida 32306, United States;* Present Address: National Center for Toxicological Research, Food and Drug Administration, Jefferson, AR 72079, USA

https://doi.org/10.1021/jacs.2c12032
J. Am. Chem. Soc. 2023, 145, 4570−4582

Valle Palomo − *Department of Chemistry, The Scripps Research Institute, La Jolla, California 92037, United States;* Present Address: Instituto Madrileño de Estudios Avanzados en Nanociencia (IMDEA Nanociencia). C/ Faraday 9, 28049 Madrid, Spain.; orcid.org/0000-0002-1473-4086

Jesse V. Jokerst − *Department of NanoEngineering, Materials Science and Engineering Program, and Department of Radiology, University of California, San Diego, La Jolla, California 92093, United States;* orcid.org/0000-0003-2829-6408

Philip E. Dawson − *Department of Chemistry, The Scripps Research Institute, La Jolla, California 92037, United States;* orcid.org/0000-0002-2538-603X

Qing-Xiang Amy Sang − *Department of Chemistry and Biochemistry, Florida State University, Tallahassee, Florida 32306, United States;* orcid.org/0000-0001-8828-0569

Complete contact information is available at: https://pubs.acs.org/10.1021/jacs.2c12032

Notes

The authors declare no competing financial interest.

■ ACKNOWLEDGMENTS

The authors thank FSU and the National Science Foundation (NSF-CHE, Grant #2005079), AFOSR (Grant no. FA9550-18-1-0144), and Kasei-Asahi Corporation for financial support. J.V.J. acknowledges support from NSF funding under award 1845683 and NIH funding under award P30 NS047101. We also thank Prof. Hong Li, Dr. Margaret Seavy, Dr. Umesh Goli, and Yizhuang Tong for the fruitful discussions.

■ REFERENCES

(1) Vandenbroucke, R. E.; Libert, C. Is there new hope for therapeutic matrix metalloproteinase inhibition? *Nat. Rev. Drug Discovery* **2014**, *13*, 904−927.

(2) Quirós, P. M.; Langer, T.; López-Otín, C. New roles for mitochondrial proteases in health, ageing and disease. *Nat. Rev. Mol. Cell Biol.* **2015**, *16*, 345−359.

(3) Kessenbrock, K.; Plaks, V.; Werb, Z. Matrix metalloproteinases: regulators of the tumor microenvironment. *Cell* **2010**, *141*, 52−67.

(4) Aoki, T.; Yonezawa, K.; Ohuchi, E.; Fujimoto, N.; Iwata, K.; Shimada, T.; Shiomi, T.; Okada, Y.; Seiki, M. Two-step sandwich enzyme immunoassay using monoclonal antibodies for detection of soluble and membrane-associated human membrane type 1-matrix metalloproteinase. *J. Immunoassay Immunochem.* **2002**, *23*, 49−68.

(5) Langer, J.; Novikov, S. M.; Liz-Marzán, L. M. Sensing using plasmonic nanostructures and nanoparticles. *Nanotechnology* **2015**, *26*, 322001.

(6) Chung, E. Y.; Ochs, C. J.; Wang, Y.; Lei, L.; Qin, Q.; Smith, A. M.; Strongin, A. Y.; Kamm, R.; Qi, Y.-X.; Lu, S.; Wang, Y. Activatable and Cell-Penetrable Multiplex FRET Nanosensor for Profiling MT1-MMP Activity in Single Cancer Cells. *Nano Lett.* **2015**, *15*, 5025−5032.

(7) Braun, A.; Farber, M. J.; Klase, Z. A.; Berget, P. B.; Myers, K. A. A cell surface display fluorescent biosensor for measuring MMP14 activity in real-time. *Sci. Reports* **2018**, *8*, 5916.

(8) Sun, L.; Chen, Y.; Chen, F.; Ma, F. Peptide-based electrochemical biosensor for matrix metalloproteinase-14 and protein-overexpressing cancer cells based on analyte-induced cleavage of peptide. *Microchem. J.* **2020**, *157*, 105103.

(9) Lakowicz, J. R., *Principles of Fluorescence Spectroscopy*. 3rd ed.; Springer: New York, 2006; 954 p.

(10) Medintz, I. L.; Mattoussi, H. Quantum dot-based resonance energy transfer and its growing application in biology. *Phys. Chem. Chem. Phys.* **2009**, *11*, 17−45.

(11) Cheng, Y.; Borum, R. M.; Clark, A. E.; Jin, Z.; Moore, C.; Fajtová, P.; O'Donoghue, A. J.; Carlin, A. F.; Jokerst, J. V. A Dual-Color Fluorescent Probe Allows Simultaneous Imaging of Main and Papain-like Proteases of SARS-CoV-2-Infected Cells for Accurate Detection and Rapid Inhibitor Screening. *Angew. Chem., Int. Ed.* **2022**, *61*, No. e202113617.

(12) Scholes, G. D. Long-Range Resonance Energy Transfer in Molecular Systems. *Annu. Rev. Phys. Chem.* **2003**, *54*, 57−87.

(13) Moroz, P.; Jin, Z.; Sugiyama, Y.; Lara, D. A.; Razgoniaeva, N.; Yang, M.; Kholmicheva, N.; Khon, D.; Mattoussi, H.; Zamkov, M. Competition of Charge and Energy Transfer Processes in Donor−Acceptor Fluorescence Pairs: Calibrating the Spectroscopic Ruler. *ACS Nano* **2018**, *12*, 5657−5665.

(14) Algar, W. R.; Malonoski, A.; Deschamps, J. R.; Blanco-Canosa, J. B.; Susumu, K.; Stewart, M. H.; Johnson, B. J.; Dawson, P. E.; Medintz, I. L. Proteolytic Activity at Quantum Dot-Conjugates: Kinetic Analysis Reveals Enhanced Enzyme Activity and Localized Interfacial "Hopping". *Nano Lett.* **2012**, *12*, 3793−3802.

(15) Medintz, I.; Clapp, A.; Brunel, F.; Tiefenbrunn, T.; Tetsuo Uyeda, H.; Chang, E.; Deschamps, J.; Dawson, P.; Mattoussi, H. Proteolytic activity monitored by fluorescence resonance energy transfer through quantum-dot-peptide conjugates. *Nat. Mater.* **2006**, *5*, 581−589.

(16) Snee, P. T. Semiconductor quantum dot FRET: Untangling energy transfer mechanisms in bioanalytical assays. *TrAC - Trends Anal. Chem.* **2020**, *123*, 115750.

(17) Oh, E.; Liu, R.; Nel, A.; Gemill, K. B.; Bilal, M.; Cohen, Y.; Medintz, I. L. Meta-analysis of cellular toxicity for cadmium-containing quantum dots. *Nat. Nanotechnol.* **2016**, *11*, 479−486.

(18) Dussert, F.; Wegner, K. D.; Moriscot, C.; Gallet, B.; Jouneau, P.-H.; Reiss, P.; Carriere, M. Evaluation of the Dermal Toxicity of InZnP Quantum Dots Before and After Accelerated Weathering: Toward a Safer-By-Design Strategy. *Front. Toxicol.* **2021**, *3*, 636976.

(19) Hardman, R. A toxicologic review of quantum dots: toxicity depends on physicochemical and environmental factors. *Environ. Health Perspect.* **2006**, *114*, 165−172.

(20) Saha, K.; Agasti, S. S.; Kim, C.; Li, X.; Rotello, V. M. Gold nanoparticles in chemical and biological sensing. *Chem. rev.* **2012**, *112*, 2739−2779.

(21) Zheng, J.; Yang, R.; Shi, M.; Wu, C.; Fang, X.; Li, Y.; Li, J.; Tan, W. Rationally designed molecular beacons for bioanalytical and biomedical applications. *Chem. Soc. Rev.* **2015**, *44*, 3036−3055.

(22) Zhou, W.; Gao, X.; Liu, D.; Chen, X. Gold Nanoparticles for In Vitro Diagnostics. *Chem. Rev.* **2015**, *115*, 10575−10636.

(23) Heuer-Jungemann, A.; Feliu, N.; Bakaimi, I.; Hamaly, M.; Alkilany, A.; Chakraborty, I.; Masood, A.; Casula, M. F.; Kostopoulou, A.; Oh, E.; Susumu, K.; Stewart, M. H.; Medintz, I. L.; Stratakis, E.; Parak, W. J.; Kanaras, A. G. The Role of Ligands in the Chemical Synthesis and Applications of Inorganic Nanoparticles. *Chem. Rev.* **2019**, *119*, 4819−4880.

(24) Wu, D.; Zhou, J.; Creyer, M. N.; Yim, W.; Chen, Z.; Messersmith, P. B.; Jokerst, J. V. Phenolic-enabled nanotechnology: versatile particle engineering for biomedicine. *Chem. Soc. Rev.* **2021**, *50*, 4432−4483.

(25) Jin, Z.; Mantri, Y.; Retout, M.; Cheng, Y.; Zhou, J.; Jorns, A.; Fajtova, P.; Yim, W.; Moore, C.; Xu, M.; Creyer, M. N.; Borum, R. M.; Zhou, J.; Wu, Z.; He, T.; Penny, W. F.; O'Donoghue, A. J.; Jokerst, J. V. A Charge-Switchable Zwitterionic Peptide for Rapid Detection of SARS-CoV-2 Main Protease. *Angew. Chem., Int. Ed.* **2022**, *61*, No. e202112995.

(26) Pons, T.; Medintz, I. L.; Sapsford, K. E.; Higashiya, S.; Grimes, A. F.; English, D. S.; Mattoussi, H. On the Quenching of Semiconductor Quantum Dot Photoluminescence by Proximal Gold Nanoparticles. *Nano Lett.* **2007**, *7*, 3157−3164.

(27) Singh, M. P.; Strouse, G. F. Involvement of the LSPR Spectral Overlap for Energy Transfer between a Dye and Au Nanoparticle. *J. Am. Chem. Soc.* **2010**, *132*, 9383−9391.
(28) Swierczewska, M.; Lee, S.; Chen, X. The design and application of fluorophore-gold nanoparticle activatable probes. *Phys. Chem. Chem. Phys.* **2011**, *13*, 9929−9941.
(29) Yang, M.; Moroz, P.; Jin, Z.; Budkina, D. S.; Sundrani, N.; Porotnikov, D.; Cassidy, J.; Sugiyama, Y.; Tarnovsky, A. N.; Mattoussi, H.; Zamkov, M. Delayed Photoluminescence in Metal-Conjugated Fluorophores. *J. Am. Chem. Soc.* **2019**, *141*, 11286−11297.
(30) Chen, C.; Hildebrandt, N. Resonance energy transfer to gold nanoparticles: NSET defeats FRET. *TrAC - Trends Anal. Chem.* **2020**, *123*, 115748.
(31) Park, S. Y.; Lee, S. M.; Kim, G. B.; Kim, Y.-P. Gold nanoparticle-based fluorescence quenching via metal coordination for assaying protease activity. *Gold Bull* **2012**, *45*, 213−219.
(32) Hutter, E.; Maysinger, D. Gold-nanoparticle-based biosensors for detection of enzyme activity. *Trends Pharmacol. Sci.* **2013**, *34*, 497−507.
(33) Kapur, A.; Aldeek, F.; Ji, X.; Safi, M.; Wang, W.; Del Cid, A.; Steinbock, O.; Mattoussi, H. Self-Assembled Gold Nanoparticle−Fluorescent Protein Conjugates as Platforms for Sensing Thiolate Compounds via Modulation of Energy Transfer Quenching. *Bioconjugate Chem.* **2017**, *28*, 678−687.
(34) Breger, J. C.; Oh, E.; Susumu, K.; Klein, W. P.; Walper, S. A.; Ancona, M. G.; Medintz, I. L. Nanoparticle Size Influences Localized Enzymatic Enhancement—A Case Study with Phosphotriesterase. *Bioconjugate Chem.* **2019**, *30*, 2060−2074.
(35) Aldeek, F.; Safi, M.; Zhan, N.; Palui, G.; Mattoussi, H. Understanding the Self-Assembly of Proteins onto Gold Nanoparticles and Quantum Dots Driven by Metal-Histidine Coordination. *ACS Nano* **2013**, *7*, 10197−10210.
(36) Fleming, A.; Cursi, L.; Behan, J. A.; Yan, Y.; Xie, Z.; Adumeau, L.; Dawson, K. A. Designing Functional Bionanoconstructs for Effective In Vivo Targeting. *Bioconjugate Chem.* **2022**, *33*, 429−443.
(37) Liu, S.; Chen, G.; Prasad, P. N.; Swihart, M. T. Synthesis of Monodisperse Au, Ag, and Au−Ag Alloy Nanoparticles with Tunable Size and Surface Plasmon Resonance Frequency. *Chem. Mater.* **2011**, *23*, 4098−4101.
(38) Jin, Z.; Du, L.; Zhang, C.; Sugiyama, Y.; Wang, W.; Palui, G.; Wang, S.; Mattoussi, H. Modification of Poly(maleic anhydride)-Based Polymers with H2N−R Nucleophiles: Addition or Substitution Reaction? *Bioconjugate Chem.* **2019**, *30*, 871−880.
(39) Jin, Z.; Sugiyama, Y.; Zhang, C.; Palui, G.; Xin, Y.; Du, L.; Wang, S.; Dridi, N.; Mattoussi, H. Rapid Photoligation of Gold Nanocolloids with Lipoic Acid-Based Ligands. *Chem. Mater.* **2020**, *32*, 7469−7483.
(40) Mei, B. C.; Susumu, K.; Medintz, I. L.; Mattoussi, H. Polyethylene glycol-based bidentate ligands to enhance quantum dot and gold nanoparticle stability in biological media. *Nat. Protocols* **2009**, *4*, 412.
(41) Jokerst, J. V.; Lobovkina, T.; Zare, R. N.; Gambhir, S. S. Nanoparticle PEGylation for imaging and therapy. *Nanomedicine* **2011**, *6*, 715−728.
(42) Jin, Z.; Yeung, J.; Zhou, J.; Cheng, Y.; Li, Y.; Mantri, Y.; He, T.; Yim, W.; Xu, M.; Wu, Z.; Fajtova, P.; Creyer, M. N.; Moore, C.; Fu, L.; Penny, W. F.; O'Donoghue, A. J.; Jokerst, J. V. Peptidic Sulfhydryl for Interfacing Nanocrystals and Subsequent Sensing of SARS-CoV-2 Protease. *Chem. Mater.* **2022**, *34*, 1259−1268.
(43) Bartczak, D.; Kanaras, A. G. Preparation of Peptide-Functionalized Gold Nanoparticles Using One Pot EDC/Sulfo-NHS Coupling. *Langmuir* **2011**, *27*, 10119−10123.
(44) Graham, C. K.; Frances, W.; Gillian, M. A novel coumarin-labelled peptide for sensitive continuous assays of the matrix metalloproteinases. *FEBS Lett.* **1992**, *296*, 263−266.
(45) Kridel, S. J.; Sawai, H.; Ratnikov, B. I.; Chen, E. I.; Li, W.; Godzik, A.; Strongin, A. Y.; Smith, J. W. A Unique Substrate Binding Mode Discriminates Membrane Type-1 Matrix Metalloproteinase from Other Matrix Metalloproteinases. *J. Biol. Chem.* **2002**, *277*, 23788−23793.
(46) Neumann, U.; Kubota, H.; Frei, K.; Ganu, V.; Leppert, D. Characterization of Mca-Lys-Pro-Leu-Gly-Leu-Dpa-Ala-Arg-NH2, a fluorogenic substrate with increased specificity constants for collagenases and tumor necrosis factor converting enzyme. *Anal. Biochem.* **2004**, *328*, 166−173.
(47) Medintz, I. L.; Clapp, A. R.; Brunel, F. M.; Tiefenbrunn, T.; Tetsuo Uyeda, H.; Chang, E. L.; Deschamps, J. R.; Dawson, P. E.; Mattoussi, H. Proteolytic activity monitored by fluorescence resonance energy transfer through quantum-dot−peptide conjugates. *Nat. Mater.* **2006**, *5*, 581.
(48) Dietz, M. S.; Wehrheim, S. S.; Harwardt, M.-L. I. E.; Niemann, H. H.; Heilemann, M. Competitive Binding Study Revealing the Influence of Fluorophore Labels on Biomolecular Interactions. *Nano Lett.* **2019**, *19*, 8245−8249.
(49) Liu, X.; Atwater, M.; Wang, J.; Huo, Q. Extinction coefficient of gold nanoparticles with different sizes and different capping ligands. *Colloids Surf. B Biointerfaces* **2007**, *58*, 3−7.
(50) Thrailkill, K. M.; Moreau, C. S.; Cockrell, G.; Simpson, P.; Goel, R.; North, P.; Fowlkes, J. L.; Bunn, R. C. Physiological matrix metalloproteinase concentrations in serum during childhood and adolescence, using Luminex Multiplex technology. *Clin. Chem. Lab. Med.* **2005**, *43*, 1392−9.
(51) Pieper-Fürst, U.; Kleuser, U.; Stöcklein, W. F.; Warsinke, A.; Scheller, F. W. Detection of subpicomolar concentrations of human matrix metalloproteinase-2 by an optical biosensor. *Anal. Biochem.* **2004**, *332*, 160−167.
(52) Vandooren, J.; Itoh, Y. Alpha-2-Macroglobulin in Inflammation, Immunity and Infections. *Front. immunol.* **2021**, *12*, 803244.
(53) Wang, W.; Ji, X.; Du, L.; Mattoussi, H. Enhanced Colloidal Stability of Various Gold Nanostructures Using a Multicoordinating Polymer Coating. *J. Phys. Chem. C* **2017**, *121*, 22901−22913.
(54) Perng, W.; Palui, G.; Wang, W.; Mattoussi, H. Elucidating the Role of Surface Coating in the Promotion or Prevention of Protein Corona around Quantum Dots. *Bioconjugate Chem.* **2019**, *30*, 2469−2480.
(55) Ji, X.; Wang, W.; Mattoussi, H. Effects of separation distance on the charge transfer interactions in quantum dot-dopamine assemblies. *Phys. Chem. Chem. Phys.* **2015**, *17*, 10108−10117.
(56) Jin, Z.; Ling, C.; Li, Y.; Zhou, J.; Li, K.; Yim, W.; Yeung, J.; Chang, Y.-C.; He, T.; Cheng, Y.; Fajtová, P.; Retout, M.; O'Donoghue, A. J.; Jokerst, J. V. Spacer Matters: All-Peptide-Based Ligand for Promoting Interfacial Proteolysis and Plasmonic Coupling. *Nano Lett.* **2022**, *22*, 8932−8940.
(57) Claussen, J. C.; Malanoski, A.; Breger, J. C.; Oh, E.; Walper, S. A.; Susumu, K.; Goswami, R.; Deschamps, J. R.; Medintz, I. L. Probing the Enzymatic Activity of Alkaline Phosphatase within Quantum Dot Bioconjugates. *J. Phys. Chem. C* **2015**, *119*, 2208−2221.
(58) Jin, Z.; Dridi, N.; Palui, G.; Palomo, V.; Jokerst, J. V.; Dawson, P. E.; Sang, Q.-X.; Mattoussi, H. Quantum Dot-Peptide Conjugates as Energy Transfer Probe for Sensing the Proteolytic Activity of Matrix Metalloproteinase-14. *Anal. Chem.* **2023**, *95*, 2713−2722.
(59) Xu, F.; Ding, H. A new kinetic model for heterogeneous (or spatially confined) enzymatic catalysis: Contributions from the fractal and jamming (overcrowding) effects. *Appl. Catal., A* **2007**, *317*, 70−81.
(60) Hens, Z.; Martins, J. C. A Solution NMR Toolbox for Characterizing the Surface Chemistry of Colloidal Nanocrystals. *Chem. Mater.* **2013**, *25*, 1211−1221.
(61) Zhang, C.; Jin, Z.; Zeng, B.; Wang, W.; Palui, G.; Mattoussi, H. Characterizing the Brownian Diffusion of Nanocolloids and Molecular Solutions: Diffusion-Ordered NMR Spectroscopy vs Dynamic Light Scattering. *J. Phys. Chem. B* **2020**, *124*, 4631−4650.
(62) Schurr, J. M. The role of diffusion in enzyme kinetics. *Biophys. J.* **1970**, *10*, 717−727.
(63) Hu, J.; Wen, C.-Y.; Zhang, Z.-L.; Xie, M.; Xie, H.-Y.; Pang, D.-W. Recognition Kinetics of Biomolecules at the Surface of Different-Sized Spheres. *Biophys. J.* **2014**, *107*, 165−173.

(64) Atkins, P. W.; De Paula, J.; Keeler, J. *Atkins' Physical Chemistry*, 11th ed.; Oxford University Press: New York, 2018, p 908.
(65) Wu, C.-S.; Lee, C.-C.; Wu, C.-T.; Yang, Y.-S.; Ko, F.-H. Size-modulated catalytic activity of enzyme−nanoparticle conjugates: a combined kinetic and theoretical study. *Chem. Comm.* **2011**, *47*, 7446−7448.
(66) Tadepalli, S.; Wang, Z.; Slocik, J.; Naik, R. R.; Singamaneni, S. Effect of size and curvature on the enzyme activity of bionanoconjugates. *Nanoscale* **2017**, *9*, 15666−15672.
(67) Vertegel, A. A.; Siegel, R. W.; Dordick, J. S. Silica Nanoparticle Size Influences the Structure and Enzymatic Activity of Adsorbed Lysozyme. *Langmuir* **2004**, *20*, 6800−6807.
(68) Petkova, G. A.; Záruba, K.; Žvátora, P.; Král, V. Gold and silver nanoparticles for biomolecule immobilization and enzymatic catalysis. *Nanoscale Res. Lett.* **2012**, *7*, 287.
(69) Lata, J. P.; Gao, L.; Mukai, C.; Cohen, R.; Nelson, J. L.; Anguish, L.; Coonrod, S.; Travis, A. J. Effects of Nanoparticle Size on Multilayer Formation and Kinetics of Tethered Enzymes. *Bioconjugate Chem.* **2015**, *26*, 1931−1938.
(70) Saha, B.; Saikia, J.; Das, G. Correlating enzyme density, conformation and activity on nanoparticle surfaces in highly functional bio-nanocomposites. *Analyst* **2015**, *140*, 532−542.
(71) Ding, S.; Cargill, A. A.; Medintz, I. L.; Claussen, J. C. Increasing the activity of immobilized enzymes with nanoparticle conjugation. *Curr. Opin. Biotechnol.* **2015**, *34*, 242−250.
(72) Malanoski, A. P.; Breger, J. C.; Brown, C. W.; Deschamps, J. R.; Susumu, K.; Oh, E.; Anderson, G. P.; Walper, S. A.; Medintz, I. L. Kinetic enhancement in high-activity enzyme complexes attached to nanoparticles. *Nanoscale Horiz* **2017**, *2*, 241−252.
(73) Vranish, J. N.; Ancona, M. G.; Oh, E.; Susumu, K.; Medintz, I. L. Enhancing coupled enzymatic activity by conjugating one enzyme to a nanoparticle. *Nanoscale* **2017**, *9*, 5172−5187.
(74) Vranish, J. N.; Ancona, M. G.; Oh, E.; Susumu, K.; Lasarte Aragonés, G.; Breger, J. C.; Walper, S. A.; Medintz, I. L. Enhancing Coupled Enzymatic Activity by Colocalization on Nanoparticle Surfaces: Kinetic Evidence for Directed Channeling of Intermediates. *ACS Nano* **2018**, *12*, 7911−7926.
(75) Jin, Z.; Kapur, A.; Wang, W.; Diaz Hernandez, J. D.; Thakur, M.; Mattoussi, H. The dual−function of lipoic acid groups as surface anchors and sulfhydryl reactive sites on polymer−stabilized QDs and Au nanocolloids. *J. Chem. Phys.* **2019**, *151*, 164703.
(76) Zhang, C.; Palui, G.; Zeng, B.; Zhan, N.; Chen, B.; Mattoussi, H. Non-Invasive Characterization of the Organic Coating of Biocompatible Quantum Dots Using Nuclear Magnetic Resonance Spectroscopy. *Chem. Mater.* **2018**, *30*, 3454−3466.
(77) Armbruster, D. A.; Pry, T. Limit of blank, limit of detection and limit of quantitation. *Clin. Biochem. Rev.* **2008**, *29 Suppl 1*, S49−52.

Recommended by ACS

Apoptosis-Amplified Assembly of Porphyrin Nanofiber Enhances Photodynamic Therapy of Oral Tumor
Xiaoyang Liu, Gaolin Liang, *et al.*
MARCH 28, 2023
JOURNAL OF THE AMERICAN CHEMICAL SOCIETY
READ

Semisynthetic Approach to the Analysis of Tumor Suppressor PTEN Ubiquitination
Reina Iwase, Philip A. Cole, *et al.*
MARCH 10, 2023
JOURNAL OF THE AMERICAN CHEMICAL SOCIETY
READ

Narrow Near-Infrared Emission from InP QDs Synthesized with Indium(I) Halides and Aminophosphine
Ranjana Yadav, Peter Reiss, *et al.*
MARCH 03, 2023
JOURNAL OF THE AMERICAN CHEMICAL SOCIETY
READ

Photon-Controlled Pyroptosis Activation (PhotoPyro): An Emerging Trigger for Antitumor Immune Response
Mingle Li, Jong Seung Kim, *et al.*
MARCH 07, 2023
JOURNAL OF THE AMERICAN CHEMICAL SOCIETY
READ

Get More Suggestions >

https://doi.org/10.1021/jacs.2c12032
J. Am. Chem. Soc. 2023, 145, 4570−4582